Image optimization for chemical species tomography with an irregular and sparse beam array

Image optimisation for chemical species tomography with an irregular and sparse beam array

N Terzija[1], J L Davidson[1], C A Garcia-Stewart[1], P Wright[1], K B Ozanyan[1], S Pegrum[2], T J Litt[3] and H McCann[1]
[1] School of Electrical and Electronic Engineering, University of Manchester, UK,
[2] Roush Technologies Ltd, Brentwood, UK, [3] AOS Technology Ltd, Melton Mowbray, UK.

Email : Natasa.Terzija@manchester.ac.uk

Abstract. High-speed tomographic imaging of hostile engineering processes using absorption-based measurements presents a number of difficulties. In some cases, these challenges include severe limitations on the number of available measurement paths through the subject, and the process of designing the geometrical arrangement of those paths for best imaging performance. This paper considers the case of a chemical species tomography system based on near-IR spectroscopic absorption measurements, intended for application to one cylinder of a multi-cylinder production engine. Some of the results, however, are applicable also to other hard-field tomographic modalities in applications where similar constraints may be encountered. A hitherto unreported design criterion is presented for optimal beam geometry for imaging performance, resulting in an irregular array with only 27 measurement paths through the subject for the engine application. Image reconstruction for this severely limited geometry is considered at length, using both simulated and experimental phantom data. Novel methods are presented for the practical generation of gaseous phantoms for calibration and testing of the system. The propane absorption coefficient at 1700nm is measured. Quantitative imaging of propane plumes in air is demonstrated, showing good localisation of circular plumes with diameter as small as 1/5 of the subject diameter and excellent imaging of multiple plumes.

Keywords: image reconstruction, imager, hard-field tomography, limited view

1. Introduction.

For many years, research has been conducted into chemically selective optical tomography based on the principle of spectroscopic absorption by the target molecules. Examples include the imaging of methane (Santoro *et al* 1981), chlorine (Faris and Byer 1986), nitrogen (Faris and Byer 1987), acetone vapour (Yost *et al* 1994), sulphur hexafluoride (Drescher *et al* 1996), helium (Feng *et al* 2002a), water (Salem *et al* 2005), and long-chain hydrocarbons (Hindle *et al* 2001, Gillet *et al* 2004).

We have recently reported on the use of the technique for high-speed imaging of hydrocarbon fuel vapour within one cylinder of multi-cylinder internal combustion engine (Wright *et al* 2005a, 2007). In addition to the more obvious problems of temperature, pressure and vibration, this application places very severe constraints on both the number and positioning of measurement paths (beams) through the subject. In particular, the need to retain the basic structural and thermal behaviour of the engine, and the proximity of the adjacent cylinder, preclude the placement of optical elements in some locations. Even in the comparatively favourable environment of single cylinder engines, previous studies (Barrag and Lawton 1993, Kramer *et al* 1998) have been restricted to no more than eight beam paths. An irregular, and almost certainly sparse, arrangement of beams is therefore characteristic of the application and any image reconstruction approach chosen must address this. Even if a spatially regular measurement grid were possible in an engine, the ability to perform image reconstruction based on a (generally irregular) subset of beams is of great value in this application; transient loss of individual beams, e.g. due to obscuration by thick films of oil or unburned fuel, is a frequent occurrence.

Limited-view tomography has been considered quite extensively in the medical imaging literature but is essentially an incomplete data problem, in so far as some projections, or parts thereof, are

unavailable within an otherwise adequately sampled system. Notable analytical studies of such problems have been provided by Andersen (1989), Verhoeven (1993), Sato *et al* (1981), and Wan *et al* (2003). The literature regarding more acutely limited cases (e.g. less than 100 path integrals) is actually very sparse. In this context, the 27-beam system used in our most recent engine studies, and others like it (e.g. Fischer *et al* 2001), can be regarded as belonging to a category of systems with severely limited data, in which both the number of viewing angles and the number of measurements are small. Image reconstruction in such situations is typically reliant upon the availability of some prior knowledge of the form of the subject (*a priori* information). Such *a priori* information (e.g. smooth variation within the subjects or knowledge of the image value in some parts of the image) can be further understood as a form of regularization. In our case, a non-negativity constraint can obviously be applied to the fuel concentration but other *a priori* information is limited. Depending upon the engine type, its running conditions and the point in the engine cycle, a wide range of fuel vapour distributions are possible, from essentially homogeneous to quite complex, with multiple local maxima. Although any spatial inhomogeneities will typically be smooth, abrupt steps can occur, particularly following fuel injection or induction events. In some instances, it may be possible to selectively apply additional constraints but, in general, the reconstruction process must proceed with little knowledge of the true form of the fuel vapour distribution.

Despite this combination of limited data and minimal *a priori* information, it is essential that the instrument responds in a predictable manner. Our adoption of a smoothness assumption (see Section 2.2) is therefore not physically motivated. Rather, it is intended to make an essentially underdetermined problem tractable, albeit at the expense of any high spatial frequency content that may be present in the underlying distribution.

In this paper we describe and test the process used to design the current 27-beam array that has been implemented on a 4-cylinder engine and the development of the associated image reconstruction algorithm. We will argue here that it is inappropriate to consider these problems in isolation as the sampling of the physical space determines our knowledge of the sinogram space and, ultimately, our ability to reconstruct successfully. Also presented here is a controlled laboratory validation of the resulting measurement grid, as subsequently used in the engine. The engine test results are described in Wright *et al* (2007).

In general, tomographic image reconstruction algorithms can be divided into two groups: iterative and non-iterative. The latter are numerically simple and computationally fast, but they can only be used to provide qualitative images. Various iterative algorithms have been developed to improve image quality and to provide quantitative images. Established techniques for image reconstruction include both series expansion algorithms and transform-based algorithms. Verhoeven (1993) made a comparative study of five well-known algorithms for limited-view problems, covering iterative and non-iterative, series expansion and transform-based approaches, and exploiting *a priori* information. It was concluded that the best performing algorithm in terms of good image quality and speed of convergence was the multiplicative algebraic reconstruction technique (MART), an iterative approach that allows the use of *a priori* information at each iteration step. Medoff *et al* (1983) developed an iterative convolution backprojection algorithm, estimating the missing projections in the sinogram space (see section 2.1). Andersen (1989) and Subbarao *et al* (1997) introduced methods similar to Medoff's, using the iterative algebraic reconstruction technique (ART) and other algebraic methods. The ART technique was used by Barrag and Lawton (1993). Other researchers (Feng *et al* 2002b, Stark *et al* 1981, Peng and Stark 1989) have performed angular interpolation between the projections in the Fourier domain. Additionally, Feng and Bao (2002b) used the smoothness of the subject as *a priori* information. Constantino *et al* (2007) have also employed methods of interpolating in the sinogram space (see section 2.1) in order to improve image reconstruction quality. Other workers (Drescher *et al* 1997, Price *et al* 2001) used the reconstruction techniques which are dependent of significant *a priori* information. These techniques reconstruct the concentration field as a trade-off between matching the measured data and regularizing the solution, by prior information, resulting in smooth images. In the cases where the distribution of concentration field is known to some extent, e.g. assuming that the concentration distribution along a plane can be written as a superposition of two-dimensional Gaussian distributions, the Smooth Basis Function Minimization (SBFM) technique developed by Drescher *et al* (1997) can be used. The Low Third Derivative method (LTD) introduced by Price *et al* (2001) calculates the concentrations with a single matrix multiplication which is

performed only once for a certain optical and prior information setup. In the LTD method, one prior information is that the third-derivative is assumed to be close to zero, resulting in locally quadratic concentration profiles. Besides these techniques, there are other image reconstruction concepts based on entropy formulation (Smith *et al* 1991, Gull and Newton 1986), where each projection is combined with an entropy function and the problem optimized with respect to maximum entropy. This approach was also used by Kramer *et al* (1998).

Early research in our laboratory employed ART for image reconstruction from 32 beams in a regular arrangement of four projections, each with 8 parallel beams (Hindle *et al* 2001). Subsequently, novel reconstruction algorithms for this system have been reported in (Garcia-Stewart *et al* 2003, Wright *et al* 2005a), including (a) the case where interpolation was performed in the linear dimension between beams within each projection and in the angular direction between projections (i.e. in the sinogram space), with filtered back projection and iteration, and (b) exploration of the use of spatial filter-based approaches that did not exploit any regular geometric relationship between beams, in conjunction with iteration. Within each iteration, *a priori* information was applied, in terms of further smoothing (by either of the methods above) and asserting non-negativity constraints. That work employed the Landweber iteration method that was initially applied to process tomography problems by Yang *et al* (1999), and has been found to be robust for small numbers of measurement data.

The paper is organized as follows: section 2 deals with the irregular and sparse beam geometry of system considered here, and describes the enhanced Landweber image reconstruction algorithm, since they are strongly coupled. Section 3 presents the necessary details of the measurement system and of the experimental procedures for homogeneous propane and propane plume measurements. Experimental validation of the overall imaging system, including quantitative calibration and estimation of the propane absorption coefficient, are presented in Section 4. Concluding remarks are given in section 5.

2. Measurement geometry design and image reconstruction

The choice of image reconstruction algorithm is not independent of the choice of beam geometry arrangement. In particular, the choice of numerical parameters for some methods may be critically dependant of the properties of the beam array. Generally, to achieve the best image reconstruction results, the measurement space should be sampled evenly in spatial and angular dimensions (Rattey and Lindgren 1981). Regular beam arrangements are often impractical in particular applications, including the multi-cylinder engine case studied here. The question then arises, given a limited set of possible sampling geometries in a given application, which of them is most suited for image reconstruction? To the best of the authors' knowledge, there is no literature available which addresses randomly sampled problems along with guidance on any associated design criteria.

2.1 Beam arrangement

One way of visualizing the properties of any beam geometry is to plot the position of all the beams in the so-called sinogram (or Radon) space, which is a two-dimensional space described by one linear variable, s, and one angular variable, θ. In the sinogram space, each beam can be represented by a single point (s, θ), where s is the length of its perpendicular distance from the origin when drawn in normal cartesian coordinates, and θ is the angle that it subtends to the vertical cartesian axis. We believe that the sinogram space representation of a given beam geometry can provide valuable insight into its potential sensitivity coverage. Figure 1(a) shows a measurement space sampled using four projections of eight beams, as used by Hindle *et al* (2001) for laboratory tests. The sampling of the physical space is regular in both the angular and linear dimensions; the resulting sinogram plot (also regular) is shown in figure 1(b).

Given the impracticality of such a regular grid in a real engine, our initial efforts were directed at maximising the number of beams, subject to the limits imposed by the physical size of the collimators and the available regions of the cylinder wall. The resulting 32-beam irregular measurement grid is shown in figure 1(c). Performance simulation of this grid, using a set of phantoms intended to represent the full range of possible in-cylinder conditions, yielded disappointing results. In seeking to maximise the number of beams, the arrangement of figure 1(c) uses typically small angles between adjacent collimators, so as to make efficient use of the available cylinder wall space. This tends to

produce adjacent beams with relatively similar (s, θ) and so leads to clustering of the beam positions within the sinogram space (figure 1(d)).
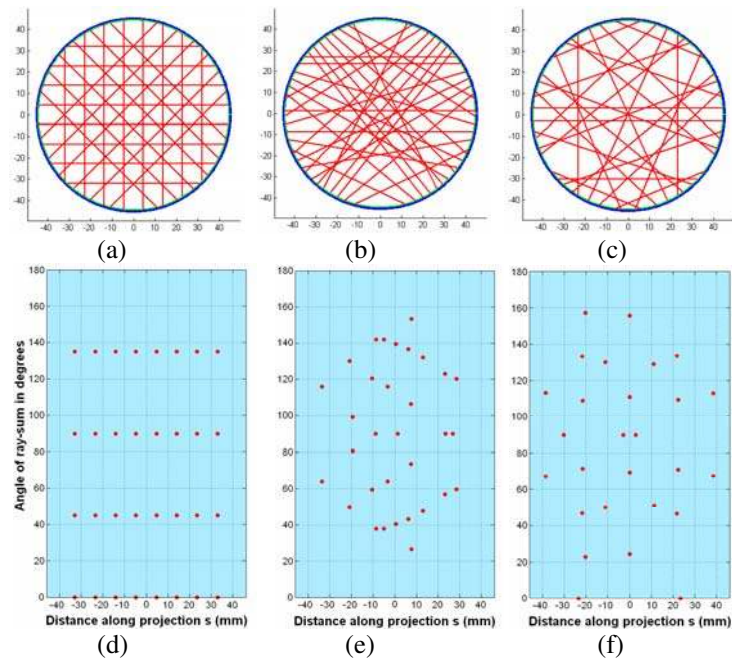

Figure 1. Three limited beam arrangements and the associated sinogram plots. Beam arrangements are for; (a) 32-beam regular geometry, (c) 32-beam irregular and un-optimized geometry and (e) reconstruction optimized irregular 27-beam geometry. The corresponding sinogram plots are shown in (b, d and f) respectively.

Although it is trivial to propose alternative 32-beam grids that are better balanced in terms of s and θ, and therefore more uniformly sampled in the sonogram space, these are unlikely to be viable solutions in practice if they disregard the mechanical constraints. In order to develop the desired ranges in s and θ, we found it necessary to reduce the number of beams, thus allowing additional space for positioning of optical elements. Short chord paths, for example, are particularly expensive in terms of usage of the combustion chamber perimeter but correspond to (otherwise unobtainable) information at high s values, i.e. close to the cylinder wall.

Simulation was carried out on a number of candidate grids, of which the best performing was that shown in figure 1(e). The simulations included hard-edged (top hat), soft-edged (Gaussian) and homogeneous phantoms to represent the full range of expected conditions. Despite having only 27 beams, this arrangement showed more consistent performance than that in figure 1(c), which we believe is due to the improved coverage of (s, θ) as evidenced by the sinogram plot (figure 1(f)). We believe that, in this case at least, the deficiencies of the arrangement in figure 1(c) are more apparent from the sinogram plot than from the physical space representation, making the former a valuable aid to the design process.

It is surprising that an apparent reduction in the available data, in an already severely limited data situation, can improve the quality of the resulting image reconstructions. However, beams that are closely spaced in s and θ traverse similar regions of physical space and they become essentially repeated measures of a single point in the sinogram space. In the uniformly sampled case, all beams contribute equally to the reconstruction process. In contrast to this, the redundancy that may be present in irregular arrangements means that the effective data gathering capability of a grid may not vary linearly, or even monotonically, with the number of beams. For this reason, the spatial distribution of beams is just as important as their number. We find the sinogram representation of the measurement grid itself to be useful in understanding these issues.

2.2 Image reconstruction

The quality of reconstructed images from sparse data sets usually suffers from fuzziness, loss of resolution and the presence of artefacts (Feng and Bao 2002b, Andersen 1989). This is due to the highly ill-posed and undetermined nature of the problem; small changes are amplified, leading to inaccurate image representation. A traditional approach to overcome limited data problems, involves the interpolation of missing projections prior to solving the inverse Radon transform. The use of transform-based inversion techniques is only applicable to beam arrangements described by projections arranged at regularly spaced viewing angles, with each projection comprising many ray-sums. In the case where the beam arrangement is not described in such a regular manner, use of a transform technique is not viable. Additionally, relatively little is known about the concentration distributions within an engine pre-combustion. For this reason, it is desirable that the image reconstruction method is capable of reconstructing a wide variety of distributions including hard-edged, soft-edged (Gaussian) and homogeneous distributions. Therefore it was decided to use a reconstruction technique which is independent of significant *a priori* information. The adopted algorithm is based on an enhanced iterative Landweber method. This technique offers generality and it has the interesting feature that it can be modified in order to take into account additional *a priori* information about the solution, such as smoothness of the subject and value constraints within each iteration. A smoothing process can provide the regularization necessary to render the inherently ill-posed problem tractable. A non-negativity constraint was also applied to maintain physically meaningful concentrations.

The algorithm is shown schematically in figure 2 and is implemented in Matlab on a standard PC. The first two steps of the algorithm are presented in greater detail in figure 3. The 27-beam measurement geometry is presented in figure 3(a), while figure 3(b) shows the corresponding circular imaging space as a subset of a 50 x 50 Cartesian grid. The sensitivity map $\mathbf{S}$ in figure 3(c) is based on calculation of the exact pixel to beam intersection lengths throughout all the pixels and for all beams. This means that some pixels which are crossed by several beams will have greater magnitude in the sensitivity map compared to those pixels which are only partially crossed by a beam. The beams in our measurement system are less than 1mm wide. Since the beams pass through only a small fraction of pixels in the imaging space, the sensitivity map is very sparse.

Considering the sensitivity map $\mathbf{S}$, an initial estimate $\mathbf{g}_1$ used for the Landweber method is found by solving the forward problem:

$$\mathbf{g}_1 = \mathbf{S}^T \mathbf{v} \tag{1}$$

where $\mathbf{g}_1$ is the estimate of concentration distribution vector $\mathbf{c}$ in each of N pixels in the imaging space, $\mathbf{v}$ is the measurement vector of L independent measurements, $\mathbf{S}^T$ is the N x L transpose of the sensitivity matrix which is here used as an approximation to $\mathbf{S}^{-1}$, and $\mathbf{S}$ is defined from $\mathbf{v} = \mathbf{Sc}$.

The iterative Landweber method can be described as:

$$\mathbf{g}_{k+1} = \mathbf{g}_k + \alpha \mathbf{S}^T \left(\mathbf{v} - \mathbf{S}\mathbf{g}_k \right) \tag{2}$$

where k is the iterative step number, $\mathbf{g}$ represents the solution in the image space and α is the relaxation parameter. An upper limit for α can generally be determined from (Yang *et al* 1999):

$$0 < \alpha < 2 \left(\left\| \mathbf{S}^T \mathbf{S} \right\|_2 \right)^{-1} \tag{3}$$

where the bracketed term is the reciprocal of the Euclidean matrix norm.

The method repeatedly compares the original measurements with those that would be expected with the updated estimate $\mathbf{g}_k$ of the concentration distribution. As long as the current approximation of the solution $\mathbf{g}_k$ is not close to the true solution, the residual $\left(\mathbf{v} - \mathbf{S}\mathbf{g}_k \right)$ is quite large and the data error is negligible as compared to the size of the residual. As the iteration process continues the value of the residual decreases while the data error component gradually increases. As shown in figure 2, the non-negativity constraint is applied by setting all the calculated negative values of the solution $\mathbf{g}_{k+1}$ to zero within each iteration. Additionally, the median filter which uses a window of specific size is applied in order to regularize the solution and to provide a degree of smoothing appropriate to typical subjects for the required image resolution. By this mechanism, the estimate of each pixel value

in the solution $\mathbf{g}_{k+1}$ is determined by the median value of the neighboring pixels within the median filter window. This is further discussed in section 4.1.2.
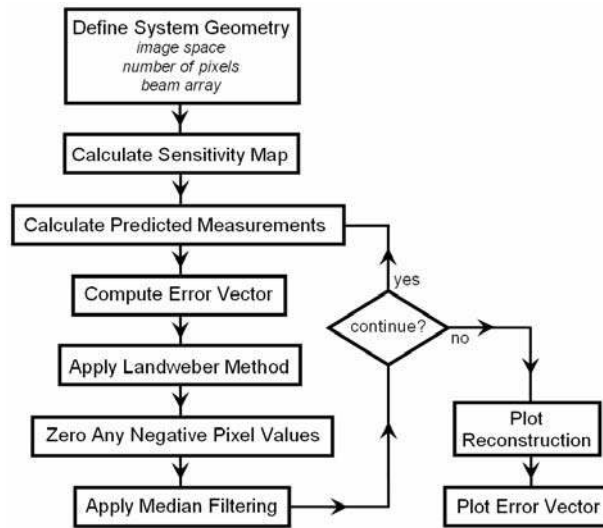

Figure 2. Schematic of the Landweber method which applies median filtering and value contraints.
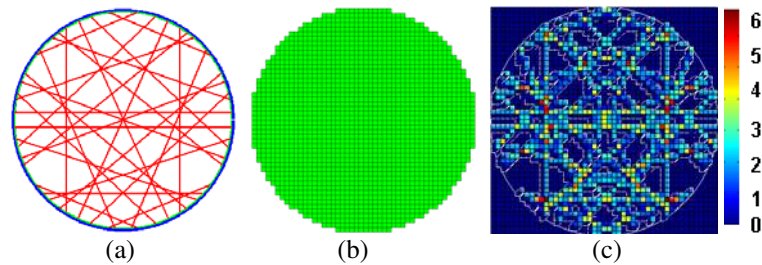

Figure 3. Defining the imaging space for the 27 beam geometry: (a) system geometry; (b) image solution space; (c) sensitivity map.

Iterative techniques widely use the residual to define a practical convergence criterion. Here the mean normalized difference e between the current and previous solution, calculated by

$$e = \left\| \mathbf{g}_{k+1} - \mathbf{g}_k \right\| / \left\| \mathbf{g}_k \right\| \tag{4}$$

is used to stop the iteration process when it is less than a predetermined threshold. In the case of our measurement system it was found that consistent results were obtained using threshold values between 1% and 4%.

Suitable selection of α continues to be a matter of great interest in tomography research. Large values of α lead to rapid convergence but increase the risk of instability. Conversely, small values of α provide slow but reliable convergence. For this reason, our initial efforts to reconstruct laboratory data have used relaxation parameters ranging from 0.001 to 0.01.

Various simulated data were used to test the effectiveness of the reconstruction method and to investigate the effect of varying reconstruction input parameters. Such parameters included: the number of pixels in the image space, the window filtering size, number of iterations, and the relaxation parameter, α. The main aim of using simulated data was to perform a simple initial assessment of the enhanced Landweber technique prior to a more thorough evaluation using real experimental data. Simulations consisted of single and double inhomogeneities describing absorption phantoms either by hard or soft edges. Typical examples are shown in figure 4 using 27 beams and applying 20 iterations. Figure 4(a-c) refers to a hard-edged inhomogeneity positioned approximately in the 2 o'clock position which gave a maximum absorption of approximately 5% to a small subset of the total number of beams. Figure 4(d-f) shows an example using two hard-edged inhomogeneities. In this case, the first phantom positioned towards 4 o'clock presents twice the absorption of the second phantom in the 10

o'clock position. Finally, figure 4(g-i) gives a typical example using a hard-edged inhomogeneity with a second soft-edged inhomogeneity towards the 8 o'clock position being simply defined by a cosine function. For this simulation, the maximum presented absorption of the soft-edged phantom was 50% compared with that of the hard-edged phantom. Similar simulations using the same enhanced Landweber reconstruction method have also used Gaussian shaped inhomogeneities and have been reported by Constantino *et al* (2007). In all cases, our reconstructions strongly suggest that the adopted reconstruction method has the ability to give good sensitivity and spatial resolution using a highly sparse and irregular beam array.
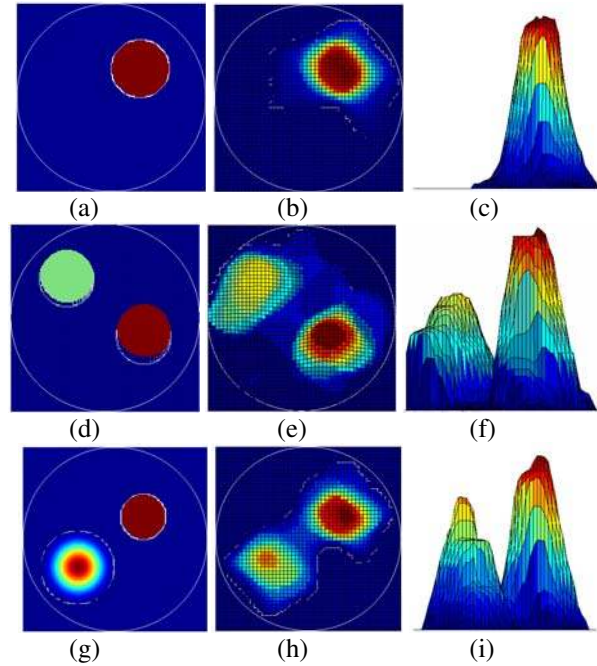

Figure 4. Typical examples of image reconstruction using the described enhanced Landweber method and simulated data. The initially generated inhomogeneities are shown in the left column, whilst the associated reconstructions are shown in the middle (plan view) and right (side view) columns. All reconstructions use 20 iterations and the IMAGER 27 beam arrangement.

3. Experimental methods

3.1 Tomography instrumentation and OPAL

The opto-electronics system developed for the IMAGER project is described more fully elsewhere (Wright *et al* 2005a). The optical interface comprises an **OP**tical **A**ccess **L**ayer (OPAL), which defines the measurement beam layout within the engine, and a rack-mounted optoelectronic measurement system. The sensing field diameter, D, of the OPAL was 89 mm. Collimation optics within the OPAL control the launch and acceptance angles sufficiently well to allow hard-field reconstruction, even in the presence of significant scattering. A dual wavelength ratiometric transmission measurement (T_{1700nm} / T_{1651nm}) is implemented on each measurement path using current-modulated diode laser sources driving a 2 by 32 fibre coupler. The dual wavelength ratiometric technique developed by Hindle *et al* (2001) is used throughout this paper. Although the OPAL used in this study featured 27 optical channels, only 26 were operational during these tests. The data reported here were time-averaged over 4ms.

3.2 Homogeneous propane-air mixture measurements

In order to assess the performance of the OPAL under homogeneous conditions, a clamping block arrangement was constructed which enabled the OPAL to be stressed in a way similar to placement of the OPAL in an internal combustion engine block. Experiments using such an arrangement allow for

an evaluation of the coupling efficiency between all optical transmission and receive channels in a well-controlled environment, over ranges of pressure and temperature. The sensing field was filled with a known homogeneous mixture of propane and air to allow the relevant absorption coefficient to be determined. Additionally, such experimental data can be compared with predicted data in order to provide calibration constants for image reconstruction which takes into account the measured differences in coupling efficiencies across all 27 beams. Such knowledge is necessary for quantitative image reconstruction.

The OPAL and the clamping block arrangement are shown in figure 5. The clamping system consists of four blocks, each measuring 180 x 250 mm^2 and 30 mm in thickness. The sensing end of the OPAL was sandwiched between the blocks (two below and two above) using a pair of standard engine metal gasket seals compressed by a clamping torque typical of an engine bolt down. The two outermost blocks were machined from aluminium, and each housed 3 electrical rod heating elements, whilst the 2 innermost blocks were machined from steel. The heating elements were positioned equidistantly along the short axis of the aluminium blocks, so as to provide uniform heating of the outer faces of the innermost steel blocks. This arrangement provided an essentially isothermal sensing field. The lower steel block included an internally drilled hole to allow pressure relief via a safety valve. The upper steel block featured two smaller internal channels to provide inlet and outlet ports for the filling gas. The whole arrangement was mounted on four cylindrical aluminium supports which positioned the setup above a 100 mm high bund which enabled the safe capture of any escaping propane gas (heavier than air) during gas removal from the OPAL and filling lines. The OPAL positioned on the two lower blocks prior to clamping down can be seen in figure 5(a) which also clearly shows the relief valve. Figure 5(b) shows the completed setup with wiring to the electrical heating elements being clearly visible.

A number of experiments investigated the effect of varying propane concentration (at fixed temperature) on the optical measurement data. Initially, the clamping block arrangement and all gas flow lines were purged with compressed air followed by filling with propane gas to a concentration level of 100%. Experiments were carried out for a total of 15 concentrations over a range starting from the initial 100% fill of propane down to an estimated 0.2% of propane. Each concentration within the range was achieved via successive dilutions of the previous concentration with compressed air. During these experiments the temperature of the setup was measured to be 34°C with approximately 1°C uniformity.
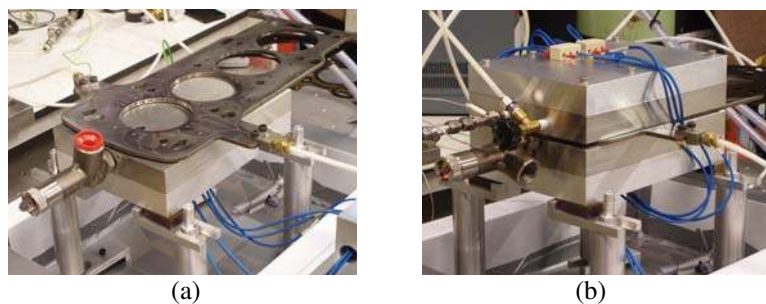

| (a) | (b) |

Figure 5. Arrangement for homogeneous propane measurements showing (a) initial build up with the OPAL positioned on the two lower clamping blocks, and (b) fully built arrangement as used for homogeneous measurements.

3.3 Propane plume measurements

The spatial resolution of the system was tested using various diameters of propane plume, either singly or in pairs. Near laminar flow plumes, of circular cross-section, were generated using a plenum chamber, diffuser and flow conditioning nozzle, suspended just above the OPAL as shown in figure 6(a). Available nozzle configurations included D/3, D/4, D/5 and combinations thereof e.g. figure 6(b). The OPAL itself was mounted on pillars to prevent recirculation of propane through the sensing field. The plumes could be positioned as desired using an X-Y translation stage and 45° rotational indexing.
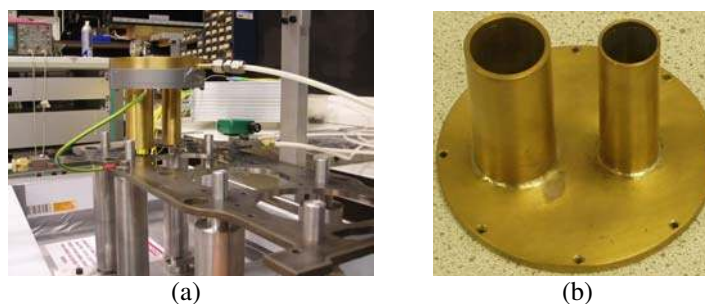
(a)   (b)

Figure 6. Arrangement for plume generation showing (a) nozzle arrangement suspended above the OPAL, and (b) close up of flow conditioning nozzle.

4. Results and discussion.

The objective of this section is to show spatial localization of various diameters of propane plumes within the sensing field. In order to produce the quantitative image reconstruction results the absorption coefficient must be known and all parameters of the image reconstruction algorithm (e.g. relaxation parameter, number of iteration and size of the median filter) have to be appropriately selected. The analyses below show the optimisation of the image reconstruction parameters and validation of the reconstruction algorithm using the experimental data.

4.1.1 Estimation of absorption coefficient for propane

The homogeneous laboratory data (described in section 3.2) were analyzed to determine the absorption coefficient for propane at 1700nm. Figure 7 shows the measured ratio T_{1700nm}/T_{1651nm} for each of the 26 operating beams at each of the 5 homogeneous propane concentrations. In fact, measurements were taken at 15 concentrations but only 5 are shown for the sake of clarity. Most beams show the expected progressive reduction in T_{1700nm}/T_{1651nm} with increasing propane concentration, although some anomalies are evident, most obviously with beams 10, 20 and 26. These may be due in part to small changes in beam alignment that occur during each successive dilution cycle. Considering only the 100% propane data, to eliminate this possibility, and treating each individual beam path as an absorption cell it is possible to derive 26 independent estimates of the absorption coefficient. This is shown in figure 8. Once again beams 10, 20 and 26 give rise to outliers and are excluded from the subsequent calculation of the mean. Despite the substantial standard deviation (7.48) of the estimated absorption coefficient, the mean (77.7 L.mol^{-1}.m^{-1}, 1 bar, 304 K) is consistent with the 76.8 L.mol^{-1}.m^{-1} reported by Kjaergaard *et al* (1990), under broadly similar conditions (0.446 bar, 295K). From this estimated absorption coefficient the expected T_{1700nm}/T_{1651nm} value for each beam in the 100% propane case was calculated. Comparison of this experimentally derived data with our initially predicted data is shown in figure 9. The discrepancy in each case provides a useful indicator of the performance of each measurement. The absorption coefficient value found here for propane at 1 bar compares reasonably with the 127 ± 12 L.mol^{-1}.m^{-1} reported by Wright *et al* (2005b) for iso-octane at 1 bar and 353K, once the larger number of available C-H vibrations per molecule of iso-octane compared with propane is taken into account.

4.1.2 Algorithm parameter optimization

Various inhomogeneous experimental data for propane plumes (as discussed in section 3.3) were used to further validate the effectiveness of the image reconstruction technique discussed in section 2.2. The effects of varying the input parameters of the reconstruction algorithm were investigated. The measurements were taken using the 25 operating beams (beams 4 and 20 were excluded). Figure 10(a) shows the IMAGER system with 25 beams, with the corresponding sensitivity map presented in figure 10(b). All of the parameter optimization results presented here are for experimental, rather than simulated, data.

A D/5 propane plume was placed either in the centre of the sensing field or in one of four different positions around this central position, as shown in figure 10(c). Using these experimental data, three

different input parameters were considered: window size of the median filter, the relaxation parameter and the number of iterations.

Median filtering is similar to a spatial averaging filter, in that it uses a window of specified size, but a given pixel value is determined by the median (rather than the mean) of the pixel values within the window. The use of the median reduces the sensitivity to extreme values, which allows removal of erroneous values in the inverse solution without reducing the sharpness in the reconstruction. Among all tested standard window sizes (3x3, 7x7, 9x9 or 11x11), 7x7 was chosen as the most appropriate window size with respect to the 50x50 grid.
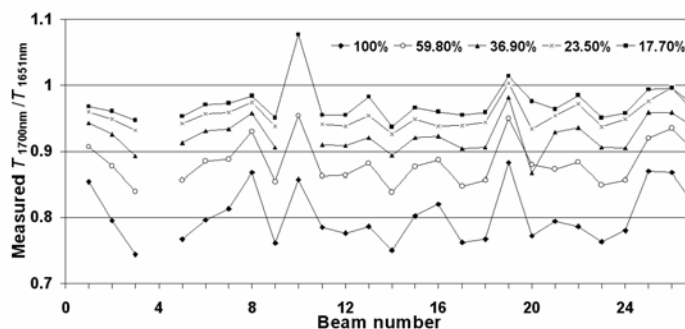

Figure 7. Measurements of T_{1700nm}/T_{1651nm}, for 26 beams of various lengths, for 100% propane at 1bar pressure and 307K temperature, and for 4 different dilutions of the propane with air, under the same homogeneous mixing and thermodynamic conditions.
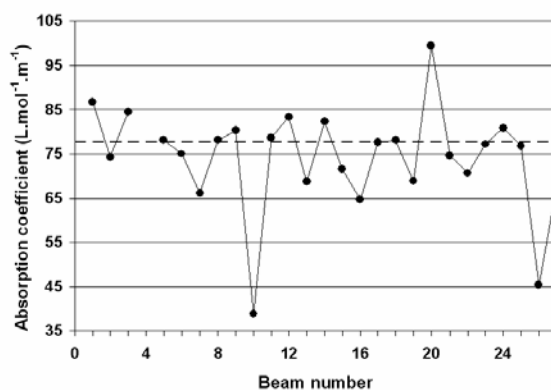

Figure 8. Estimation of the absorption coefficient for propane for each beam, derived from the 100% propane data of figure 7. The broken line corresponds to a value of 77.7 L.mol^{-1}.m^{-1}.

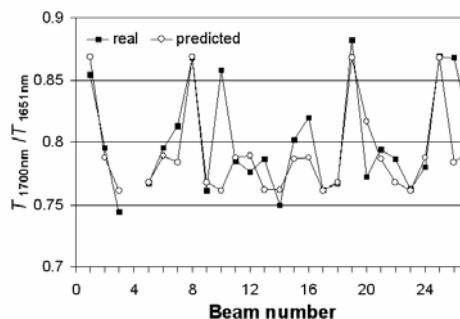**Figure 9.** Predicted ratiometric data, using the measured absorption coefficient, compared with the actual measurements obtained.

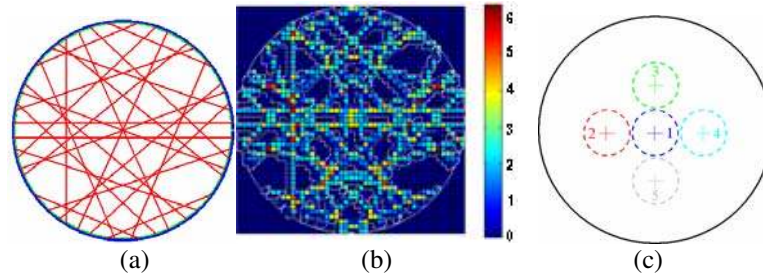(a)   (b)   (c)

Figure 10. The IMAGER beam arrangement with 25 beams, used for image reconstruction is shown in (a) whilst the corresponding sensitivity map is given in (b). Illustration of approximate D/5 plume positions are given in (c).
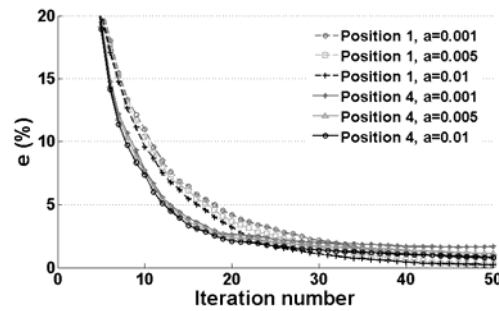

Figure 11. Normalized convergence parameter as a function of iteration number. The results for three different relaxation parameters are presented and compared.
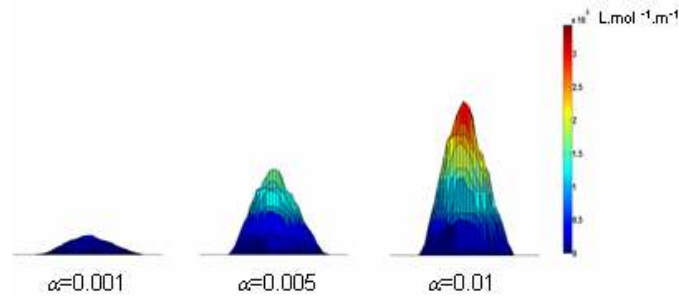

Figure 12. Image reconstruction with 25 iterations of a D/5 propane plume showing the effect of using three different relaxation parameters.

The relaxation parameter α plays an important role in the stability of the solution and speed of convergence. As a measure of convergence a relative image error (see equation 4) was adopted. Figure 11 shows the normalized convergence parameter e as a function of iterations calculated using three different relaxation parameters: 0.001, 0.005 and 0.01. Only the results for "position 1" and "position 4" are presented for clarity. It can be seen that in both cases where the relaxation parameter was set to 0.01, the convergence parameter e, reaches the threshold of 3% after 25 iterations. The influence of different relaxation parameters for 25 iterations and a 7 x 7 median filter can be seen more clearly from the actual reconstructions shown in figure 12.

4.2 Validation of image reconstruction algorithm
Figures 13-15 show the image reconstruction results for various diameters of propane plume (D/3, D/4 and D/5, where D is diameter of the sensing field). All the reconstructions use a pixel image space based on a 50 x 50 grid but the inverse solution is only calculated in the highlighted circular region which comprises 1844 pixels. This is a further attempt to improve the accuracy of solution by improving the conditioning of the problem. All these reconstructions use the same 7 x 7 median filter, the same relaxation parameter (0.01) and 25 iteration steps.

Qualitative image reconstruction results for a D/5 propane plume in each of 5 positions are shown in figure 13(a-e). The reconstructions are individually scaled to emphasise the successful localization of the single plume in each case. Quantitative reconstructions of the same data are given in figure 13(f-j), with all reconstructions globally scaled. Comparing figures 13(a-e) and 13(f-j), relatively poor sensitivity is apparent in position 5 (figure 13(j)). The origin of this lower sensitivity can be seen by comparing figure 10(b) with figure 10(c); this region of the sensitivity map is generally sparser and has fewer beam intersections than those regions of the grid relevant to figure 13(f-i).
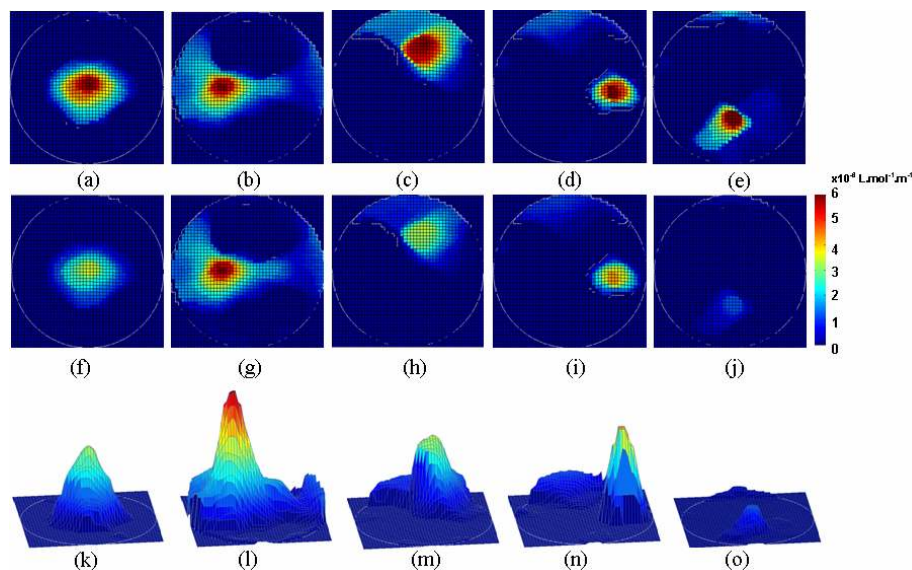

Figure13. Qualitative and quantitative image reconstructions of a D/5 propane plume in 5 different positions (see figure 10(c)). All reconstructions which are given in (a)-(j) use the same relaxation parameter 0.01, same median filtering, 25 iterations and data from 25 beams. The qualitative reconstructions, which are presented (a)-(e), are locally scaled. The quantitative reconstructions are shown in (f)-(j) whilst the corresponding profiles are given in (k)-(o). All quantitative reconstructions are globally scaled.
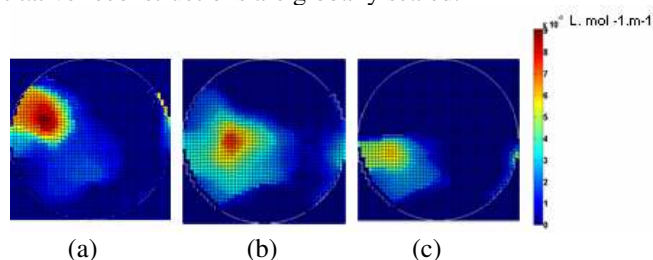

Figure 14. Quantitative image reconstructions of a D/4 propane plume in 3 different positions. In this case, the plume generator was shifted from the original position in (a) by two consecutive 10 mm increments in a vertical downward direction relative to this page. Reconstructions of these new positions are shown in (b) and (c).
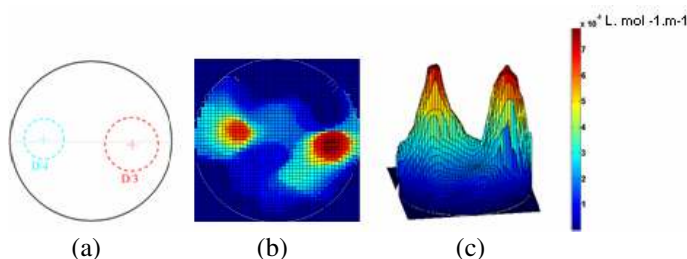

Figure 15. Quantitative image reconstruction examples of D/4 and D/3 propane plumes produced simultaneously. Approximate positions of the plumes are shown in (a) and the corresponding reconstruction is shown in (b-c).

Figure 14 shows quantitative reconstructions from measurements of single D/4 propane plume in three positions at 10 mm intervals. Good spatial localisation of the propane plume is evident. An example of the ability of the system to resolve multiple simultaneous plumes is given in figure 15. This is a quantitative reconstruction derived from measurements of an asymmetric double plume phantom (one D/4 and one D/3 plume, D/4 apart).

It can be seen from these figures that the reconstructions represent the approximate size and locality of the propane plumes with fewer artefacts than might be expected considering the highly sparse nature of the beam array.

5. Conclusions

For hard-field tomographic imaging of subjects not amenable to regular sampling geometry, the design of the array of measurement paths (beams) presents a substantial challenge. In such cases, design priority should be given to achieving the best possible coverage of the sinogram space, in both the linear and angular dimensions. A solution to this problem has been presented for the task of in-cylinder hydrocarbon fuel imaging in operating multi-cylinder gasoline engines. A reduced number of beams (27) has been adopted compared to the physically available maximum that could have been installed (32 or more), in order to improve the sinogram coverage.

For image reconstruction of the resulting data, the iterative Landweber method has been used, with regularization provided by median filtering and non-negativity constraint. A systematic study has been made of the trade-off between the value of the relaxation parameter and the number of iterations. With the chosen parameters, the image reconstruction algorithm was found to offer stable and reliable phantom localization, for both simulated and experimental data, with normalized image error values around 3% after 25 iterations.

Experimental tests were carried out on homogeneous gaseous propane at various pressures. The resulting estimate of the absorption coefficient extends the very limited published data for propane close to STP. This phase of testing also served to show that a small number (10%) of beams did not yield reliable measurements of concentration path integral, and these were excluded from imaging tests.

A method has been described for the laboratory creation of steady-state gaseous phantoms with non-uniform concentration of the target species. Quantitative images of such phantoms, each containing one or two propane plumes, have been successfully reconstructed, with good localisation being achieved for plumes ranging from 1/5 to 1/3 of the overall diameter of the phantom subject.

References

Anderson A H 1989 Algebraic reconstruction in CT from limited views *IEEE Trans. Med. Imaging* **8**(1) 50-55

Barrag A and Lawton B 1993 Computer Optical Tomography of Internal Combustion Engine Soot Concentration *Proc. 26th International Symposium Automotive Technology* 423-430

Constantino E P A, Davidson J L and Ozanyan K B 2007 Comparison of two methods for tomographic imaging from severely incomplete data *5th World Congress on Industrial Process Tomography (Bergen, Norway)*

Drescher A C, Gadgil A J, Price P N and Nazaroff W W 1996 Novel approach for tomographic reconstruction of gas concentration distributions in air: use of smooth basis functions and simulated annealing *Atmospheric Environment* **30**(6) 929-940

Faris G W and Byer R L 1986 Quantitative optical tomographic imaging of a supersonic jet *Opt. Lett.* **11** 413-415

Faris G W and Byer R L 1987 Quantitative three-dimensional optical tomographic imaging of supersonic flows *Science* **238** 1700-1702

Feng J, Okamoto K, Tsuru D, Madarame H and Fumizawa M 2002a Visualization of 3D gas density distribution using optical tomography *Chem. Eng. J.* **86**(3) 243-250

Feng J and Bao S L 2002b Reconstruction of smooth distribution within unsmooth circumferences from limited views using filtered backprojection algorithm *Int. J. Imaging Systems Technol.* **12**(3) 93-96

Fischer M L, Price P N, Thatcher T L, Schwalbe C A, Craig M J, Wood E E, Sextro R G and Gadgil A J 2001 Rapid measurements and mapping of tracer gas concentrations in a large indoor space, *Atmos. Environ,* **35** 2837–2844

Garcia-Stewart C A, Polydorides N, Ozanyan K B and McCann H 2003 Image reconstruction algorithms for high-speed chemical species tomography *3rd World Congress on Industrial Process Tomography (Banff, Canada)*

Gillet B, Hardalupas Y, Kavounides C and Taylor A M K P 2004 Infrared absorption for measurement of hydrocarbon concentration in fuel/air mixtures (MAST-B-LIQUID) *Appl. Thermal Eng.* **24** 1633-1653

Gull S F and Newton T J 1986 Maximum-entropy tomography, *Appl. Opt.,* **25** 156-160

Hindle F P, Carey S J, Ozanyan K B, Winterbone D E, Clough E and McCann H 2001 Measurement of gaseous hydrocarbon distribution by a near infra-red absorption tomography system *J. Electronic Imaging,* **10**(3) 593-600

Kjaergaard H G, Yu H, Schattka B J, Henry B and Tarr A W 1990 Intensities in local mode overtone spectra: Propane *J Chemical Physics*, **93**(9) 6239-6248

Kramer H, Einecke S, Schulz C, Sick V, Nattrass S R and Kitching J S 1998 Simultaneous mapping of the distribution of different volatility classes using tracer LIF and NIR tomography in an IC engine *SAE Trans.* **107** 1048-1059

Medoff B P, Brody W R, Nassi M and Macovski A 1983 Iterative convolution back-projection algorithms for image reconstruction from limited data *J Opt. Soc Amer.* **73** 1493-1500

Peng H and Stark H 1989 One-step image reconstruction from incomplete data in computer tomography *IEEE Trans. Med. Imaging* **8**(1) 16-31

Price P N, Fischer M L, Gadgil A J and Sextro R G 2001 An algorithm for real-time tomography of gas concentrations using prior information about spatial derivatives, *Atmos. Environ*. **35** 2827–2835

Rattey P and Lindgren A 1981 Sampling the 2-D Radon transform *IEEE Trans. on Acoustics, Speech, and Signal Processing* **29**(5) 994 - 1002

Salem K, Tsotsas E and Mewes D 2005 Tomographic measurements of breakthrough in a packed bed adsorber, *Chem. Eng. Sci.* **60** 517-522

Santoro R J, Semerjian H G, Emmerman P J and Goulard R 1981 Optical tomography for flow field diagnostics *Int. J. Heat Mass Transfer* **24**(7) 1139-1150

Sato T, Norton S J, Linzer M, Ikeda O and Hirama M 1981 Tomographic image reconstruction from limited projections using iterative revisions in image and transform spaces *Appl. Opt.* **20**(3) 395-399

Smith R T, Zoltani C K, Klem G J and Coleman M W 1991 Reconstruction of tomographic images from sparse data sets by a new finite element maximum entropy approach *Appl. Opt.* **30**(5) 573-582

Stark H, Woods J W, Paul I and Hingorani R 1981 Direct fourier reconstruction in computer tomography 1981 *IEEE Trans. Acoust. Speech, Signal Processing* **29**(2) 237-245

Subbarao P M V, Munshi P and Muralidhar K 1997 Performance of iterative tomographic algorithms applied to non-destructive evaluation with limited data *NDT&E International* **30**(6), 359-370

Verhoeven D 1993 Limited data computed tomography algorithms for physical sciences *Appl. Opt.* **32**(20) 3736-3754

Wan X, Gao Y Q, Wang Q, Le S P and Yu S L 2003 Limited-angle computed tomography algorithms *Opt. Eng.* **42**(9) 2659-2669

Wright P, Garcia-Stewart C A, Carey S J, Hindle F P, Pegrum S H, Colbourne S M, Turner P J, Hurr W J, Litt T J, Murray S C, Crossley S D, Ozanyan K B and McCann H 2005a Toward in-cylinder absorption tomography in a production engine *Appl. Opt.,* **44**(31) 6578-6592

Wright P, Ozanyan K B, Carey S J and McCann H 2005b Design of high-performance photodiode receivers for optical tomography *IEEE Sensors Journal* **5** 281-288

Wright P, Terzija N, Davidson J L, Garcia-Castillo S, Garcia-Stewart C, Pegrum S, Colbourne S, Turner P, Crossley S D, Litt T, Murray S, Ozanyan K B and McCann H 2007 High-speed Chemical Species Tomography in a multi-cylinder automotive engine *5th World Congress on Industrial Process Tomography (Bergen, Norway)* (submitted to the *Chemical Engineering Journal*, 2008)

Yang W Q, Spink D M, York T A and McCann H 1999 An image-reconstruction algorithms based on Landweber's iteration method for electrical-capacitance tomography *Meas. Sci. Technol.* **10** 1065-9

Yost M G, Gadgil A J, Drescher, Zhou Y, Simonds M A, Levine S P, Nazaroff W W and Saisan P A 1994 Imaging indoor tracer-gas concentrations with computed tomography: experimental results with a remote sensing FTIR system *Am. Ind. Hyg. Assoc. J.* **55**(5) 395-402